CHEMISTRY
A EUROPEAN JOURNAL

DOI: 10.1002/chem.201001724

3rd EuCheMS Chemistry Congress

Model Studies in Heterogeneous Catalysis

H.-J. Freund*[a]

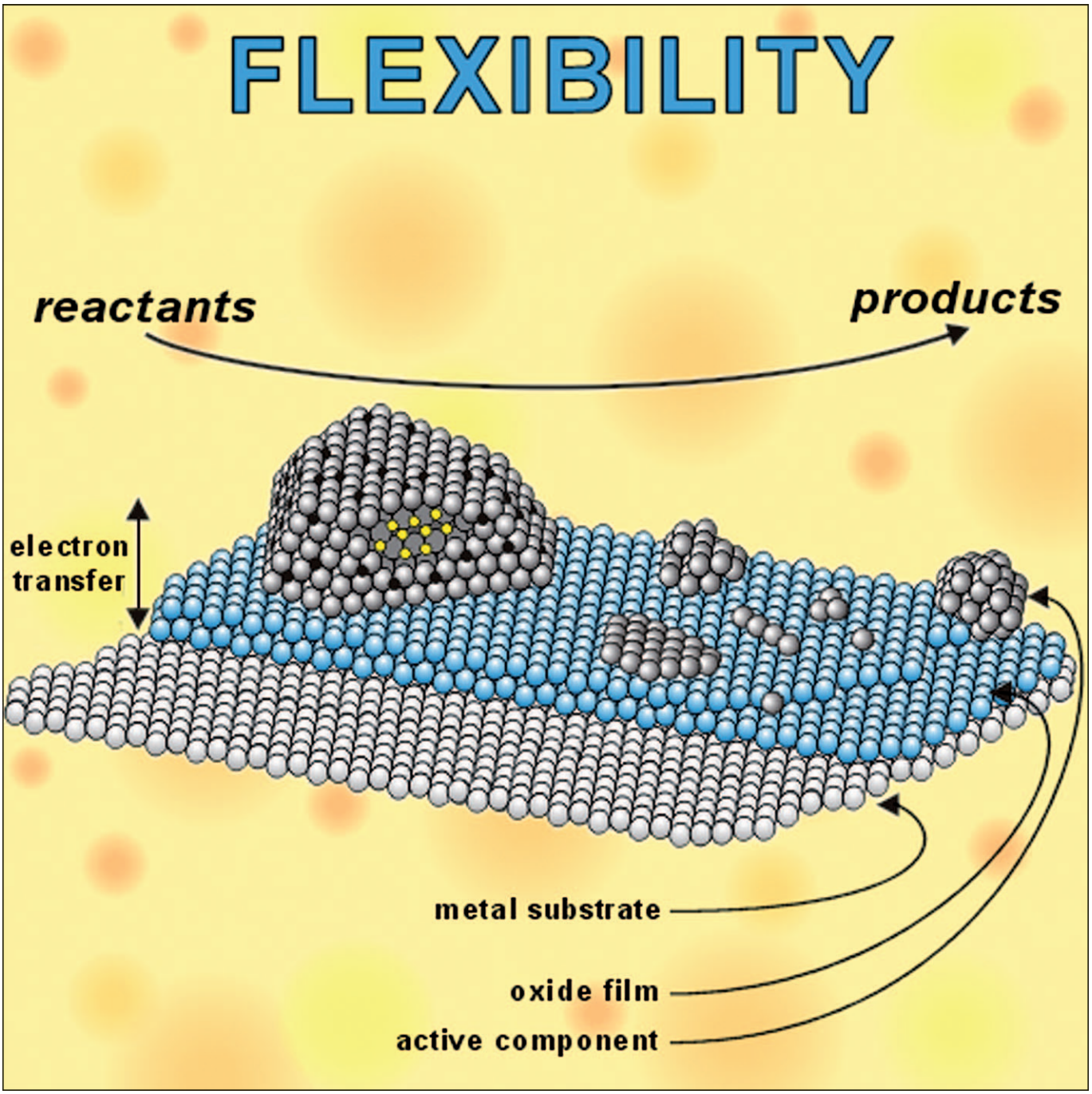

Abstract: I review a concept that models heterogeneous catalysis based on a surface-science approach. It is shown that models catching part of the complexity of the real system, which is connected with the finite size of active components and the flexibility of the arrangement of atoms in the active component, play an important part in determining the activity and selectivity of the system. I have chosen several examples from our own laboratory to elaborate the details and will put those into perspective with respect to the literature. I will show that Pd nanoparticles in hydrogenation incorporate hydrogen, which turns out to be crucial for the actual hydrogenation step. Another example correlates the structure of vanadia monolayer catalysts with its reactivity in methanol oxidation. With a third example we address the question of charge on Au nanoparticles when anchored to an oxide surface, a problem heavily discussed in the literature. Further examples refer to ultrathin oxide film catalysts in which the oxide metal interface controls either the charge state of Au particles grown on the film, and, in a last example, the oxide film itself exhibits remarkable CO-oxidation activity, which can be traced to a reactive intermediate structure of the ultrathin film.

Keywords: heterogeneous catalysis · model systems · nanoparticles · surface chemistry · ultrathin films

Introduction

Wet impregnation of supports with transition-metal salts from solution is frequently applied to prepare disperse metal catalysts.[1] The particles formed are not homogeneous in size and distribution, and are usually characterized by electron microscopy and their chemical reactivity. The use of thin, well-ordered oxide films as support materials, which do not charge up during measurement, provides materials that allow us to capture some of the complexity represented by technologically employed disperse metal catalysts, while allowing the application of the tool box of surface science to study surfaces at atomic detail.[2–13]

Figure 1 shows a schematic diagram of the kind of model systems studied and which will be addressed in the present review.[8]

There are two classes of model systems: one, in which the goal is to represent a disperse supported metal or a mixed oxide catalyst.[2–4,9–12] Both are shown on the left-hand side of Figure 1 and are based on the ability to model the bulk or volume of a supporting oxide by using thin film techniques. In a second class of model systems, shown on the right-hand side, the thickness of the oxide film and the oxide metal interface created by growing the film are used as decisive parameter to control the electronic structure.[5–8] This may influence either a supported deposit, for example, a metal atom or nanoparticle, or the film itself, by the chemical potential of the gas phase, resulting in the formation of a catalytically active phase. The phenomena observed for this second class of materials are very much influenced by the flexibility that the oxide lattice of a thin film exhibits as compared to the bulk material, and it may provide a new route to catalyst design. However, lattice flexibility is also

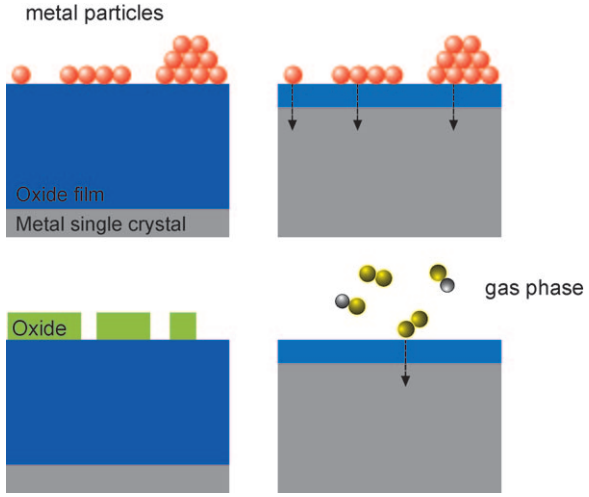

Figure 1. Schematic representation of classes of model systems.

an important ingredient to understand catalysis by supported nanoparticles, that is, the sytems shown on the right, as components of the gas phase may interact very strongly with the nanoparticles and even be incorporated into the nanoparticle at considerably lower temperature when compared with the metal bulk.

There are a number of interesting specific systems in which catalysis may be strongly connected to this aspect of flexibility, but for which it has not been considered to play a role; for example, gold catalysis, methanol synthesis, and CO oxidation over ruthenium oxide. Also, the necessity to include materials flexibility in a description of catalytic phenomena has been largely neglected in theoretical modeling of catalytic reactions, but may be necessary to reach an atomistic understanding of both the energetic and, in particular, the kinetic aspects of catalysis, which is a kinetic phenomenon, after all.

The present paper centers around this question and we will show, by virtue of several examples, how the phenomena addressed express themselves.

[a] H.-J. Freund
Fritz Haber Institute of the Max Planck Society
Department of Chemical Physics
Faradayweg 4-6, 14195 Berlin (Germany)
Fax: (+49) 30-8413-4101
E-mail: freund@fhi-berlin.mpg.de

Modeling Oxide Supported Catalysts

We start with an example in which Pd nanoparticles are deposited on a thick (≈10 nm) Fe_3O_4(111) film and we investigate the adsorption of simple molecules, such as carbon monoxide, as a function of particle size (see Figure 2).[14] It

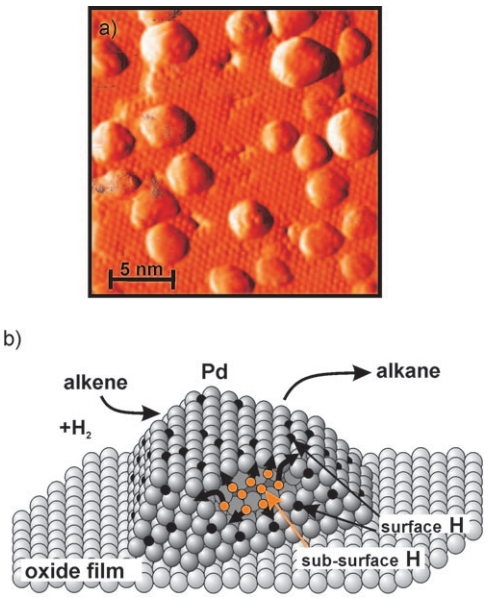

Figure 2. a) STM image of Pd nanoparticles on Fe_3O_4(111). The crystallographic facets of the particles are clearly recognizable as is the atomic corrugation of the support. b) Schematic representation of a Pd nanoparticle indicating atomic hydrogen adsorbed on the surface and in the particle.

shows an STM image of Pd nanoparticles on an Fe_3O_4(111) surface.[15,16] The particles are facetted with (111) and (100) planes, establishing truncated octaedra as schematically shown in Figure 2b.[17] For Pd on alumina it was even possible to resolve the atomic structure of the facets.[18] A problem occurs when applying the technique of temperature-programmed desorption to determine heats of adsorption of molecules in such systems, because the particles may move during the temperature ramp and agglomerate on the surface. Only in cases in which the molecules are physisorbed, so that the change in temperature to desorb the molecules is much less than the temperature to induce particle mobility, may this technique be applied successfully.[19,20] Chemisorbed molecules, or molecules that dissociate upon adsorption, need to be studied by calorimetric techniques.[21,22] Schauermann et al. have developed a single-crystal adsorption calorimeter, sufficiently sensitive to record heats of adsorption of particle ensembles with sizes of the individual particles in the range of hundred atoms.[14] This calorimeter is based on ideas developed by King et al.[21] and refined by Campbell et al.[22] for metal and oxide single crystals. Figure 3 addresses the dependence of the initial heats of adsorption on particle size for samples represented in Figure 2. The particle sizes, in fact, varied between 100 and 5000 atoms per particle on average. The dependence of the initial heat of adsorption on particle size shows a pronounced trend: it decreases with decreasing particle size from 126 to 106 kJ mol^{-1}, and is always smaller than the value measured for the Pd (111) single crystal, which is the correct reference, as the particles (Figure 2) are mainly terminated with (111) facets. Two effects are thought to contribute to this observation: the weakening of the chemisorptive bond due to the known contraction of the Pd–Pd bond length in smaller particles (bond-order conservation)[23] and also to the weakening of the van der Waals interaction due to the reduced dynamic response of the metal electrons when the particles size decreases towards fluctuations in the adsorbed molecule.[19] This measurement settles a controversy in literature (see

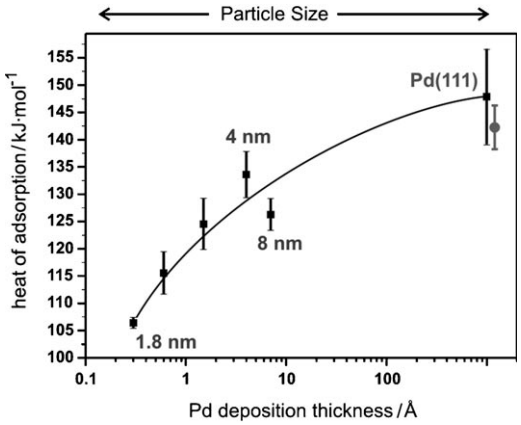

Figure 3. Initial heat of adsorption of CO as a function of Pd coverage measured on the Fe3O4/Pt(111) samples with the nominal deposition thickness of 0.3, 0.6, 1.5, 4, and 7 Å and on the Pd(111) single-crystal surface. Each point in this curve is an average of 4–6 independent measurements on freshly prepared model systems. Error bars: the standard error of the mean. The grey circle corresponds to the value of the CO adsorption heat on Pd (111) reported by Conrad and Ertl.[121]

Hans-Joachim Freund (born 1951) studied physics and chemistry at the University of Cologne and received his Ph.D. in 1978 and his habilitation in 1983 when he became Associate Professor at Erlangen University and in 1987 Professor at Bochum University. Between 1979 and 1981 he worked in the Physics Department at the University of Pennsylvania as a postdoctoral fellow. In 1995 he accepted a position as scientific member and director at the Fritz-Haber-Institut der Max-Planck-Gesellschaft in Berlin where he is head of the Department of Chemical Physics. He serves as Honorary Professor of four universities. He received several awards including the Leibniz Award/DE, the ACS Somorjai Award (US) and the Centenary Medal (UK). Since 1996 he is a member of several academies. He has published more than 500 scientific papers. He is a founding member of the Scientific Council of the European Research Council.

discussion in references [2,14]) about whether to expect a decrease or increase in the initial heats of adsorption with decreasing particle size, and it also provides benchmarks to theory, for which we are not in a position , at present, to provide accurate results including van der Walls energies for systems of this size. While in this example we have dealt with an adsorption phenomenon that, of course, represents only one elementary step in a catalytic cycle, the next example exemplifies the influence of materials flexibility on a catalytic reaction. We are studying hydrogenation of a simple hydrocarbon molecule, such as *cis*-2-butene[24–28] on exactly the same model system as shown in Figure 2. This molecule is used in order to follow certain reaction paths that would be difficult to elucidate with ethene itself, although we assume the same chemistry to apply in both cases.[17,29]

Hydrogenation of *cis*-butene on well-facetted Pd particles represents a model system, in which one would assume that a metal single-crystal approach, à la Ertl[30] or Somorjai,[31] to reactivity would perfectly apply. However, as will be outlined, this is not the case. Due to the considerably higher flexibility of the lattice of the small particle as compared with a single crystal, the interior of the particle actively participates in reactions and, in particular, in hydrogenation reactions by hydrogen accommodation at conditions different from the bulk material.[26,32–35] Here we will only briefly recapitulate the basis for this statement. First we note, that in contrast to a Pd(111) single crystal, the supported Pd nanoparticles, under molecular beam conditions, fully reproduce, within the accessible pressure regime,[36] the results known for technical catalysts.[37] We recall that hydrogenation occurs according to the Horiuti–Polanyi mechanism.[38] As shown in Figure 4 the key intermediate is represented by a species in which the C=C double bond is half hydrogenated at one end and bound to the surface at the other end, that is, in the case of *cis*-2-butene, a butyl species is formed.[39–43]

This species may than either again dehydrogenate and desorb as *trans*-2-butene, the stable isomer of *cis*-2-butene, or may be fully hydrogenated to desorb as butane. Parallel to this, the hydrocarbon may fully dehydrogenate and deposit carbonaceous species on the surface. While both isomerization and dehydrogenation are observed on the Pd(111) single crystal, the fully sustained hydrogenation reaction is not observed; however, on the nanoparticles all reactions are observed.[32,33] In addition, sustained catalytic activity has only been observed on the nanoparticles. Recently, we have demonstrated that this is connected with the presence of carbonaceous species, which influences the diffusivity of hydrogen from the surface to the sub-surface region (shown schematically in Figure 2b) of the metal.[24–27] It is the sub-surface hydrogen that turns out to be key for the hydrogenation reaction. While sub-surface hydrogen has been proposed to be crucial for both Pd single crystals and Pd nanoparticles, the volume of the Pd single crystal favors the entropy driven dissolution of hydrogen, while in a nanoparticle the hydrogen is forced to stay near the surface due to its size and the diffusion barrier of the oxide. How much of the hydrogen is present in the particle is set by the chemical potential of the gas phase, and, due to the higher flexibility of the metal nanoparticle lattice, this amount will be different from a single crystal.

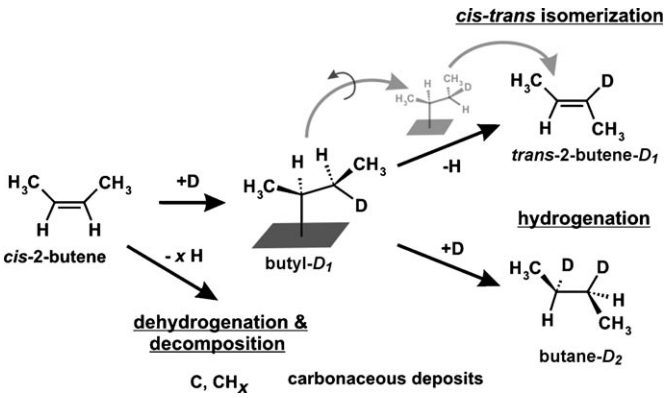

Figure 4. Schematic representation of the various steps following the Horiuti–Polanyi mechanism for alkene hydrogenation, exemplified with *cis*-butane. The key intermediate is the butyl species from which isomerization and hydrogenation branches out.

Figure 5 shows the averaged hydrogenation rates obtained from a series of pulsed molecular beam experiments, in which the catalyst was exposed to a continuous D_2 molecular beam (to differenciate from H_2 in the background) and a modulated *cis*-2-butene molecular beam at 260 K. The hydrogenation rates as a function of time on Pd(111) (upper row) and supported Pd nanoparticles (lower row) on the carbon free (black curves) and carbon containing (grey curves) surfaces are plotted in Figure 5. On both carbon-

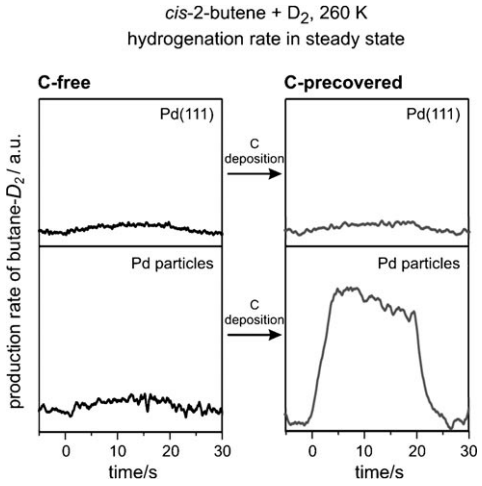

Figure 5. Averaged hydrogenation rates obtained from a series of pulsed molecular beam experiments, in which the catalyst was exposed to a continuous D_2 molecular beam and a modulated *cis*-2-butene molecular beam at 260 K. The rates were calculated by averaging the reaction rates from the last 30 long pulses of the experiment and were normalized to the number of the surface Pd atoms for quantitative comparison. Shown are the hydrogenation rates plotted as a function of time on Pd(111) (top panels) and Pd particles (bottom panels) on the C-free (left) and C-containing (right) surfaces.

free surfaces no sustained hydrogenation may be observed, while the competing *cis–trans* isomerization (not shown) proceeds effectively on both surfaces. These observations point to a limitation of the availability of sub-surface hydrogen, while there is no limitation to the availability of surface hydrogen. We have used resonant nuclear reaction analysis (r-NRA) to quantitatively determine the amount of surface versus sub-surface hydrogen in supported nanoparticles, and used that knowledge to prove the importance of the sub-surface species for the hydrogenation reaction.[26,44] One result is shown in Figure 6. Here we compare four traces in a set

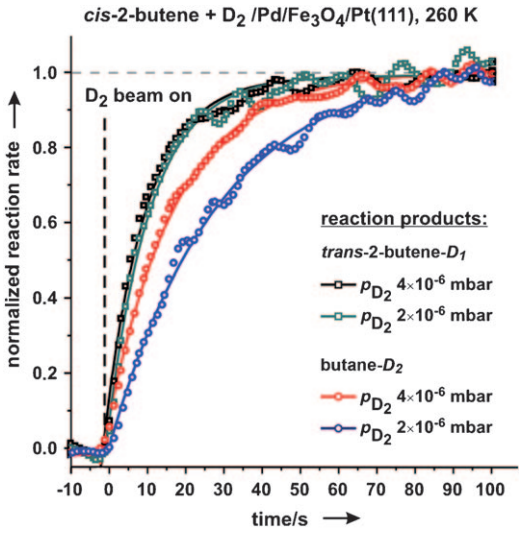

Figure 6. Results of molecular beam experiments for *cis*-2-butene isomerization as compared to hydrogenation. For details see references [25,26] and text.

of molecular beam experiments. The conditions for those experiments have been chosen based on the knowledge from r-NRA experiments that between the two hydrogen pressures the surface is saturated in hydrogen, while the hydrogen content in the particle still strongly varies. Two of the four traces monitor the isomerization reaction (*cis*-2-butene to *trans*-2-butene) and the other two the hydrogenation towards butane as recorded by mass-spectrometry. It is quite evident that the isomerization reaction, which is accepted to be a reaction driven by surface hydrogen, does not change with hydrogen pressure, as expected for saturated surface hydrogen coverage. On the other hand, the hydrogenation depends on hydrogen pressure, that is, hydrogen concentration in the particle. This clearly demonstrates the importance of this species for the hydrogenation channel.

In summary, we note on the basis of this example, that, in order to trace results observed on real catalysts, it is important to capture some of the complexity of the real system. In the present case it is the size of the metal particle and the presence of the support that is important to understand the elementary processes involved. Here, metal single crystals represent a too simple model system.

The next example is concerned with the reactivity of oxide nanoparticles supported by another oxide material. It is an established concept among catalyst scientists that so-called monolayer catalysts, in which a reactive oxide, such as vanadia, is supported on a second oxide, such as ceria, exhibits considerably higher activity for methanol oxidation towards formaldehyde. This does not mean that such catalysts may soon replace the iron molybdate based catalysts currently used in industry, but it is interesting to try to understand the monolayer catalysts on a more detailed basis and to verify some of the ideas that have been put forward in the catalysis literature. Our studies are mainly based on results reviewed by Wachs,[45] who compared vanadia overlayers on a number of support materials, such as SiO_2, Al_2O_3, ZrO_2, TiO_2, and CeO_2. Plotting the turnover for methanol oxidation to formaldehyde against the electronegativity of the support cations, he noticed a nonlinear increase from SiO_2 to CeO_2, indicating that the support may play an active role in the process. In a combined experimental and theoretical effort together with Sauer's group, we have studied these systems using the described model catalyst approach.[46–56] We have studied alumina, silica, and ceria as supports for vanadia deposits prepared by physical vapor deposition in an oxygen ambient. Briefly, vanadia grows as three-dimensional clusters, both on alumina and silica, with low to high coverage. The vanadium is present in oxidation state (+III) in the volume of the clusters and in oxidation state (+V) at the surface, as evidenced by photoelectron spectroscopy and the appearance of vanadyl vibrations, which indicate the same surface termination of the clusters as found for $V_2O_3(0001)$ surfaces.[52] These supported clusters oxidize methanol to formaldehyde at about 500 K, independent of vanadia coverage. On the basis of these studies it was possible to reassign the vibrational spectra of supported vanadia and identify vanadia-support interface vibrations that had been previously assigned to vanadyl vibrations of oligomeric vanadia deposits. While on silica and alumina three-dimensional growth of vanadia is observed, on ceria the predicted growth of monomeric, oligomeric, and two-dimensional (i.e., monolayer) vanadia is, in fact, observed and interesting correlations with spectroscopic data and reactivity may be drawn.

Figure 7 shows a combination of STM images and vibrational and photoelectron spectra for vanadia deposits on ceria. The ceria support was grown as a thin film (thick enough to represent the bulk)[57] on a Ru(0001) single-crystal surface according to a procedure described by Mullins et al.[58] and modified in our group.

A large scale image of the ceria film is shown on the far left of Figure 7. Upon deposition of small amounts of vanadia, small, statistically distributed protrusions are observed that are accompanied by an IR absorption spectrum indicative of isolated vanadyl groups. Upon increasing the coverage we see larger protrusions occurring (looking like trimers) that grow into two-dimensional islands, with even a second layer on top of them. Parallel to this, a shift of the vanadyl frequency to higher values compatible with dipolar

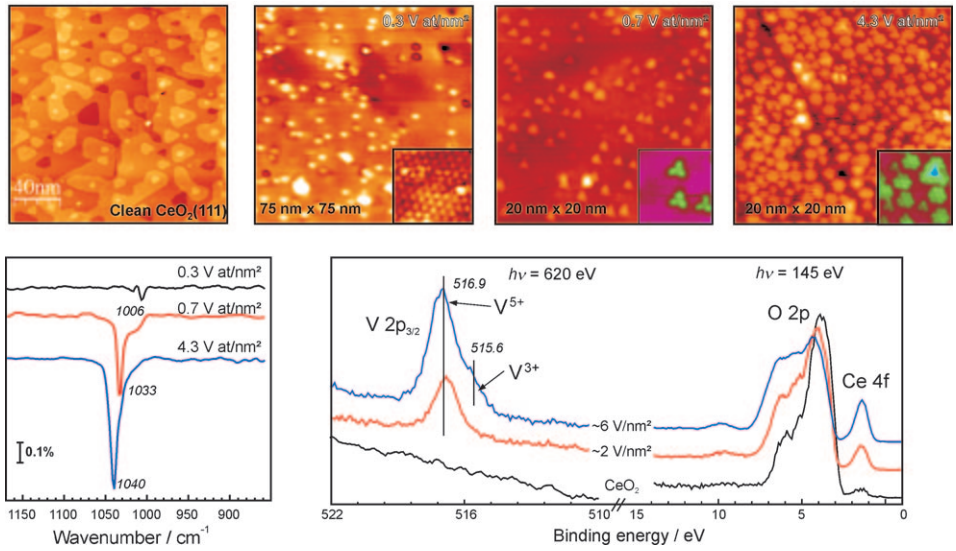

Figure 7. Top: STM images of CeO_2(111) films on Ru(0001): far left: clean; towards the right increasing coverage of vanadium per nm^2 in oxygen as given in the images. Bottom left: FTIR spectra after vanadia deposition for three different coverages. Bottom right: Photoelectron spectra before and after vanadia deposition on CeO_2(111)/Ru(0001) in the range of $V2p_{3/2}$ and the valence band ionization taken with synchrotron radiation at BESSY II.

coupling in the larger aggregates, and opposite to what was deduced from studies on powders, is observed. This is yet another example in which model studies on well-defined structures can help to settle spectroscopic assignments. The infrared spectra are indicative of the formation of vanadyl (i.e., V^{+V}) species, which is corroborated by chemical shifts in XPS spectra (see Figure 7). The higher vanadia loadings show the occurrence of V^{+III} species with the appearance of large aggregates in the STM images. It is interesting to note that parallel to this, the valence-band spectra show an increasing Ce^{+III} signal near the Fermi energy. This can easily be explained by a redox mechanism upon vanadia adsorption. As the vanadia adopts its V^{+V} oxidation state, it reduces the ceria in the film, originally in the Ce^{+IV} state, to Ce^{+III}. Note that the small Ce^{+III} signal in the clean film stems from Ce^{+III} at defects (steps and vacancies). We have studied such samples with respect to methanol oxidation to formaldehyde using temperature-programmed reactions (TPR). The outcome is interesting and is summarized in Figure 8.[55,56] While CeO_2 is itself active, producing formaldehyde near 600 K, a higher loading of vanadia produces a TPR peak below or near 500 K, similar to the larger clusters of vanadia on silica and alumina. For the monomers and small vanadia cluster species, which are not stable to high temperature, a TPR peak of considerably lower temperature (370 K) is observed. Hydrogen abstraction has been identified as the rate-limiting step in the oxidative dehydrogenation of propane and methanol.[59,60] In the case of methanol, the hydrogen atom is abstracted from a surface-bound methoxy group. One of the electrons of the dissociated C–H bond forms a CH_2O surface radical, whereas the other one is transferred with the hydrogen atom to a surface oxygen site and results in a reduced metal ion. The Bronsted–Evans–Polanyi (BEP) principle suggests a linear relationship between energy barriers and reaction energies for catalytic steps that can be decomposed into C–H bond dissociation of the surface methoxy and hydrogenation of the oxygen species. When we consider different catalysts, the former is constant and, hence, the BEP suggests a linear relationship between the energy barriers and the hydrogenation energies of the surface oxygen species. From the hydrogenation energies of the reaction given in Equation (1), together with the oxygen defect creation energy, which is necessary to consider as a water molecule is formed from the hydrogenated vanadia species

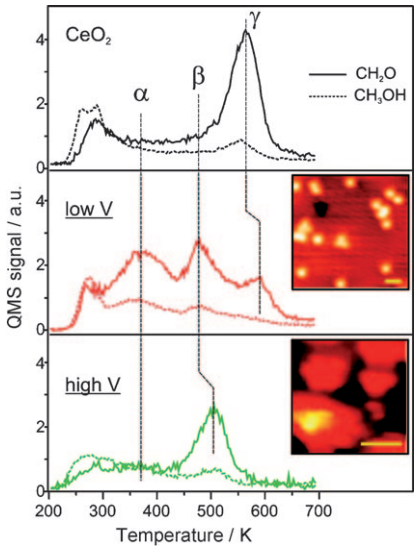

Figure 8. TPD spectra for ≈5 L of CH_3OH adsorbed at 300 K on CeO_2-(111) and VO_x/CeO_2 (111) surfaces at low (<2 V at nm^{-2}) and high (≈4 V at nm^{-2}) vanadia loadings. Solid lines indicate the raw signal for CH_2O (29 amu), whereas dashed lines indicate CH_3OH (31 amu, corrected for the methanol cracking pattern). Signal intensity below 300 K is assigned to the tail of CH_3OH monolayer desorption. The insets show typical STM images of vanadia species at the respective coverage. The scale bar corresponds to 1 nm.

[Eq. (2)], we are in a position to construct a descriptor for methanol oxidation.[59–62]

$$VO_n/CeO2(111) + {}^1\!/_2H_2 \rightarrow VO_nH/CeO_2(111) \quad (1)$$

$$VO_n/CeO_2(111) - {}^1\!/_2O_2 \rightarrow VO_{n-1}/CeO_2(111) \quad (2)$$

The more exoenergetic the hydrogenation, the higher is the catalyst's activity. It turns out, through DFT calculations by Sauer et al.,[56] that creating an oxygen vacancy on the vanadium-covered surface costs less energy than on the pristine ceria. Moreover, the electrons left on the surface are located on the ceria, leaving vanadia in its highest oxidation state. The reducibility of the ceria does not diminish with the fraction of reduced ceria ions already present, because the electrons reside in 4f orbitals that do not interact with each other.[63] This fully supports the statement above and renders species such as monomers more reactive, as is observed experimentally. In summary, this is another example in which model studies may be employed to reveal detailed structure reactivity relations, hardly possible on powder samples for which structure may be deduced, at best, rather indirectly.

Defect creation and electrons on those defects are crucially important to describe reactivity, as exemplified by the vanadia clusters on ceria and their ability to oxidize methanol. The presence of charged defects may also influence the properties of metal nanoparticles anchored to or near those defects.[64–74] We discuss here "color center" formation on Mg(100) surfaces and its influence on metal adsorption. The MgO(100) surface is prepared by growing an oxide film on either Ag(100) or Mo(100). The two systems are different with respect to the films morphology. While growth on Ag(100) leads to very smooth films due to the small lattice mismatch between Ag(100) and MgO(100), growth on Mo(100) leads to pronounced mosaic structure caused by the larger misfit. The consequence is a different behavior with respect to the stabilization of charged defects.

The best studied defects in simple oxides, such as MgO, are so-called F or color centers.[64,65,75] They represent oxygen vacancies that may trap up to two electrons. Those electrons may be excited with visible light and cause the coloring of ionic crystals, hence color centers. At the surface oxygen vacancy sites can be found at many places, for example, on a terrace, at a step or at a corner of a step, to name but a few. Due to the differing coordination of oxygen atoms in different surface sites, the energy needed for creation of vacancies differs considerably.[75] The vacancy formation energy, in general, is high, and one way of inducing defects is by using electron-stimulated desorption of oxygen. Overall, the smaller the coordination of a site is, the lower is the energy needed for vacancy creation. This is why surface vacancies are preferentially found at step and edge sites as revealed by the STM or by an AFM image in Figure 9a.[64,71] Using the STM as a spectrometer to record so-called scanning tunneling spectra, or using the scanning force microscope to record the surface potential locally, one may differentiate different types of oxygen vacancies. The available information is summarized in Figure 9b. Briefly, four different defect sites have been identified, namely, the oxygen vacancy without electrons, those with one or two electrons, and a morphological defect, a so-called negatively charged di-vacancy. Morphological defects will be addressed in more detail below.[74] The defects all show characteristic spectra in

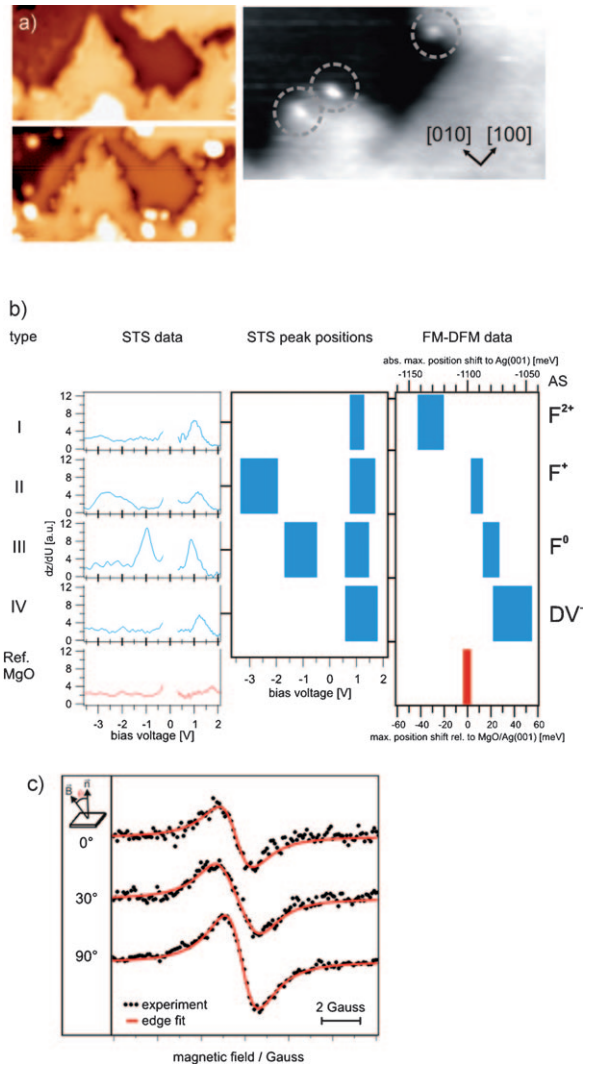

Figure 9. a) Low-temperature (4 K) STM image (28×16 nm2) of 4 monolayer thick MgO(001)/Ag(001) after electron bombardmentat U bias = +3.5 V showing the morphology of the MgO film (top left), and at U bias = −2.5 V (bottom left) showing electronic surface defects. FM-DFM image (right) taken at constant Δf showing a MgO step edge with point defects (indicated by the dashed circles). Scan range (right): 23.0×11.5 nm^2; Δf = −1.6 Hz; VS = −50 mV. b) The right labels indicate the different defect types. The left graph shows STS spectra of the respective defect. The right graph presents the maxima of the STS data. The covered abscissa range accounts for the statistics of the peak positions. The relative shift of the local potential $\Delta\Phi_{rel}$ with respect to the MgO surface (bottom abscissa) and the absolute shift $\Delta\Phi_{abs}$ with respect to the Ag(001) level (top abscissa), both shifts including the local charge. c) Experimental and simulated EPR spectra of color centers on a 20 monolayer thick MgO(001)/Mo(001). F^{2+}: doubly charged color center, F^{+}: singly charged color center, F^{0}: nutral color center, DV: divacancy.

the band gap of MgO (the spectrum is given for comparison) and also exhibit different local potentials. If both properties are considered simultaneously, a unique identification of the species is possible. For a detailed explanation of the data we refer to the original literature. Note, that by varying the electron current and energy in the electron stimulated desorption of oxygen, the abundance of the kind of defect may be varied and controlled to a certain extent. Such ex-

periments allow for defect engineering. A technique that allows for the specific detection of defects with unpaired electrons is electron spin resonance spectroscopy, which we applied to single-crystal oxide surfaces for the first time.[64] A spectrum of paramagnetic color centers on MgO(100) is shown in Figure 9c. Since the spectra are taken on a single crystal, surface-angle-dependent measurements allow for the determination of the *g* tensor components, and thus for the symmetry of the site. From a detailed analysis, an edge site and the abundance are deduced, in agreement with the observations in the STM. Morphological defects, which may be either of di-vacancy type (above) or of grain boundary type, are a special case. In the latter case they may trap electrons, actually a large number of electrons. In this case, the traps are associated with a nonstoichiometric defect composition and filled by transfer of electrons from a metal substrate, even without electron bombardment. Such defects are dominant on thin film systems in which there is a large misfit between the oxygen and the metal lattice constants. Therefore, MgO(100) on Mo(100) exposes a large number of such defects, while MgO(100) on Ag(100) does not. These experiments put us in a position to study the influence of charged defects onto the electronic structure and adsorption capabilities of metal clusters anchored to those sites. We will concentrate here on Au particles, also to provide material for comparison with results on Au nanoparticles on ultrathin MgO films, discussed below. Metal atoms, when deposited by means of physical vapor deposition, feel attracted to the defect sites, which we were able to experimentally demonstrate with an AFM experiment.[72] This attraction will lead to the nucleation of Au particles of different sizes, which may be imaged by the STM as shown in Figure 10a. In this particular case, the Au was evaporated onto a MgO(100)/Mo(100) film with a pronounced mosaic structure. The morphological defects can actually attract a fair amount of charge from the Mo(100), due to their higher local work function. We have shown from photon-STM measurements that those morphological defects may be charged by several electrons per defect and may also be discharged into the metal.[74] The Au particles in this case accumulate on those morphological defects, that is, along the mosaic grain boundaries, and attract the charge due to their high electron affinity, as shown in the STM image (Figure 10a).[73] This may be probed through adsorption of CO, the stretching frequency of which is sensitive to the charge state of the particle.[73] A very impressive series of studies on CO stretching frequencies to free clusters of varying sizes and charge (+, 0, and −) has been studied in Meijer's group and is very useful for comparison here.[76–80] In a previous publication, it was demonstrated that CO molecules adsorbed on individual Au atoms supported on MgO exhibit an enormous red shift of the stretching frequency.[81] Figure 10b shows a set of IR absorption spectra taken for such particle distributions created through varying amounts of deposited Au, increasing the Au coverage from trace a) through h). All observed bands are red shifted compared to CO adsorbed on MgO(100) itself, which gives rise to a very intense band centered around

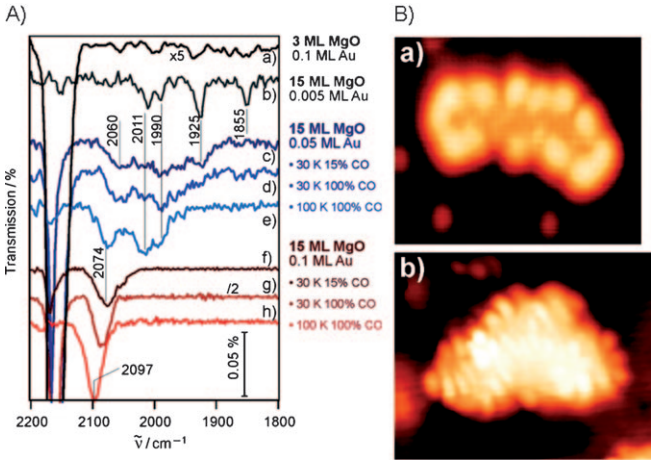

Figure 10. A) a) Infrared adsorption spectrum of CO adsorbed on a 3 monolayer (ML) thick MgO/Ag(0001) film covered with 0.1 ML Au. b)–h) IR spectra taken on an electron-bombarded 15 ML thick MgO/Mo film covered with b) 0.005 ML Au (CO saturation coverage, 100 K), c) 0.05 ML Au (15% CO exposure, 30 K), d) 0.05 ML Au (saturation coverage 30 K), and e) 0.05 ML Au (saturation coverage 100 K). The spectra f)–h) were taken for 0.1 ML Au coverage and f) 15% CO exposure (30 K), g) CO saturation coverage (30 K), and h) after annealing the sample to 100 K. B) STM topographic image of Au clusters deposited on a 12 ML thick, electron-bombarded MgO/Mo(001) film (100×100 nm2, 5.5 V, 20 pA). The aggregates preferentially nucleate at the dislocation lines in the film.

2146 cm^{-1}. At highest Au loading (spectrum h) the CO stretching frequency is only slightly shifted with respect to Au clusters on pristine MgO films on Ag(100) with very low defect density, which show stretching frequencies between 2100 and 2125 cm^{-1}. The low-frequency lines occurring at smallest metal exposure are assigned to Au atoms adsorbed on regular terrace sites (1855 cm^{-1}) and F^0 centers (1925 cm^{-1}) on the basis of earlier measurements. All other bands may be assigned to CO bound to negatively charged Au aggregates located on top of electron-rich surface defects by comparison with results from calculations. In particular, the features at 1990 and 2010 cm^{-1} at lowest Au coverage are suggested to originate from CO adsorption on dimers and trimers bound to color centers. For higher Au exposures new blue-shifted lines emerge in the frequency range around 2060 cm^{-1} that shift to 2070 cm^{-1} upon annealing to 100 K. For the highest coverage f)–h), the spectrum is dominated by a band at 2074 cm^{-1}, while the strongly red-shifted bands disappear. In general, the observed CO stretching frequencies experience a decreasing red shift with higher Au exposure and thus increasing particle sizes. It is reasonable to assume that for larger particles, the average negative charge per Au atom decreases, which leads to a smaller population of the anti-bonding CO 2π orbital and thus to a less red-shifted CO stretching frequency. With the analysis so far it is not clear where on the Au nanoparticles the CO molecules are bound. We will show below through imaging with ineleastic electron tunneling spectroscopy for comparable system on very thin films, that the CO is bound to the edge sites.

The last case study presented sheds light onto a puzzle in the literature in which it was assumed that negatively charged clusters (which are formed by mass selection in the gasphase before deposition) form on point defects on MgO(100) films on a Mo(100) substrate.[82–85] As shown above, point defects only form after electron-stimulated desorption. The abundance of point defects on materials that have not been exposed to an electron beam is so small that neither the temperature-programmed reaction data not the IR absorption spectra in the literature could have been explained. However, as demonstrated, in particular on MgO films on Mo(100)—which were used in the experiments we refer to—morphological defects form that trap electrons from the substrate without electron bombardment. It is these defects that are likely to be responsible for the negative charge on the particle as deduced by comparison with calculations. However, this is an artifact of the system studied, and is therefore not suited to claim relevance for catalysis on powder materials.

Ultrathin-Film Catalysts

We now move the discussion to the second class of systems discussed in the introduction. Here we discuss ultrathin films for which we have to consider the interaction between the adsorbate on the thin film and the metal oxide support interface.[5]

To analyze the situation with the help of simple physical models one has to consider, for example, the physical quantities that determine electron transfer from the metal substrate through the film.[86] On one hand, there is the ionization potential that excites an electron from the metal oxide, which is, in general, not simply the work function of the metal, because it will be substantially modified by the presence of the oxide overlayer, and, on the other hand, the electron affinity of the species adsorbed on the oxide surface, which again may be influenced by the interaction with the oxide surfaces. If the energy balance between those quantities results in an energy gain, then the electron transfer is possible, in principle. However, this is only part of a proper description, because it is not evident how the quantity would depend on thickness of the film, as the energy balance will only weakly depend on it for very thin films! Of course, in case of films with a thickness of several nanometers, the tunneling probability would simply be zero. But why would an oxide film of three layers differ from one of eight layers with respect to tunneling? The reason is connected with the increased lattice flexibility of very thin films, which is altered very rapidly as the film gets thicker, quickly approaching the phonon behavior of the bulk or a bulk terminating surface. In other words, a thin film has the ability to accommodate the charge accumulated through electron transfer by a lattice distortion, a property that a thick film may not exhibit. This phenomenon is called a polaronic distortion and is known from metal semiconductor physics. One may use this knowledge to choose combinations of materials in thin oxide film design to produce systems with specific electronic properties with respect to electron transfer, which may in turn lead to specific chemical reactivity. Take, for example, cations, anions or neutrals of one and the same species: They show different adsorption behavior and will undergo very different chemical reactions! Therefore, if we succeed in designing specific support systems that promote the formation of specific charge states, we might come to the point where we design catalysts for specific reactions. Of course, under reaction conditions one has to consider the presence of the gas phase as well, when we try to control the electron transfer by materials design, because the gas phase determines the chemical potential of a catalyst. It is evident that the phenomenon described, again, is a manifestation of the flexibility of the system, the unifying concept of this review.

It was Haruta[87] who reported that small gold particles, not more than 3-4 nm in size, supported on titania exhibit high catalytic activity for a number of interesting chemical reactions. For example, such systems catalyze CO oxidation already at, or even below room temperature, a result that is surprising, as Au is not known for its high chemical reactivity. This is, of course, why Au is called a noble metal. The observations by Haruta have led to many subsequent studies with the goal to unravel the reason for this high reactivity. While there is progress, the problem has not been completely settled.[6,88,89] One open question concerns the state of charge of the Au particles in its reactive state, an issue that we have addressed already in the previous chapter, showing how charging may be influenced by the presence of defects. Another question refers to the site of reaction on the Au particles. One could imagine that all Au atoms of the particles show the same reactivity, or alternatively, some specific sites could solely be responsible for the reactivity. For example, the Au atoms at the rim or circumference of the particle, which are in contact with the oxide substrate but are still accessible from the gas phase, could be candidates for such sites. To get closer to a solution, we have prepared samples with particles of varying sizes, starting from single Au atoms up to clusters containing 70 atoms or more, which is the size at which the band gap closes and a transition to metallic Au, in the classical sense, occurs on a MgO(100) film composed of three layers.

The oxide film is epitaxially grown on an Ag(001) surface, covering it completely, and its thickness was chosen such that electrons may be transferred from the MgO/Ag interface to the adsorbed Au particles. We specifically chose Ag(100) over Mo(100) for this particular study, because in the latter case, as discussed above, the electron trapping within grain boundaries determines the nucleation of metal, which we try to ovoid here.

This charge transfer reflects itself in the distribution of individual Au atoms on such an MgO(100) film as shown in Figure 11a.[90,91] The Au atoms try to avoid close contact due to their negative charge leading to interatomic repulsion. If more Au is deposited a wetting of the surfaces occurs and a variety of two-dimensional Au aggregates form, which are

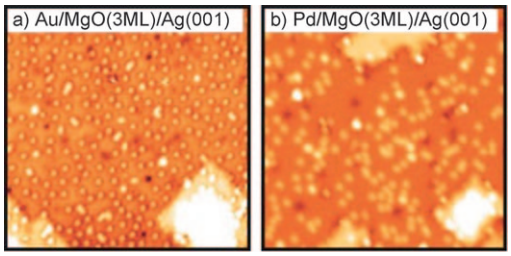

Figure 11. a) STM image of Au deposited on 3 monolayer thick MgO on Ag(001). b) STM image of Pd deposited on 3 monolayer thick MgO-(001).

stable up to room temperature.[92] Had the experiments been performed on a thick MgO(100) film, the aggregates would have grown into three-dimensional objects instead, as typically found for the growth of metals on oxides. Evidently, thin oxide films can be used as spacers to grow ideally flat metal–insulator structures at the smallest of dimensions. It is necessary to point out, and to remind us that this statement strongly depends on the system. Had we deposited Pd instead of Au onto the thin MgO film (Figure 11b), we would have observed the growth of three-dimensional objects in the end, and neutral Pd atoms at the beginning, exhibiting a regular diffusion-limited spatial distribution.[92] Therefore, the general statement, often read in literature, that thin films are not to be used as models for bulk oxide materials is very much misleading, as it is strongly dependent on the system studied.

As stated above, clusters of varying sizes were systematically studied. Au_1–Au_7 clusters, which are mainly linear and clusters with sizes from Au_{10}–Au_{20}, which are two-dimensional, have been imaged.[93,94] Some examples have been studied in detail. In Figure 12, STM images of a flat Au_{18} cluster,[95] taken at a number of different voltages, are shown. Below the images of differentiated current voltage curves (so-called scanning tunneling spectra) are plotted, for which the tip was placed at the positions indicated by colored dots the top left image. The appearance of the images evidently depends dramatically on the imaging voltage. This is a consequence of quantum mechanics that determines, of course, the electronic structure of the object. The unpaired 6s electrons of the Au atoms that constitute the cluster lead to electron wave functions of the clusters which are strongly remnant of an electron gas confined to a two-dimensional well potential. The potential and the number of electrons determine the nodes in the electron density. The Au_{18} cluster, according to the schematic structure, as is shown in the inset in Figure 12 (top middle panel), is asymmetric. If we remove the Au atom at the far right of the cluster, a symmetric Au_{17} cluster would be created. We note in passing that, indeed, the stoichiometry of a given cluster may be established by using tip manipulation techniques.[93,94] To understand the electronic structure we inspect the scanning tunneling spectra shown below the images in Figure 12. The maxima correspond to the electron distribution within cluster states, represented by the conduction images shown above the spectra. It is possible recognize the position of the nodal planes in the spatial electron distributions. Also, the asymmetry induced by the eighteenth atom is clearly visible. Based on the position of the nodes it is also evident why one does not observe all maxima in all scanning tunneling spectra: If the tip is positioned within a nodal plane, there is no current to be detected for the specific state and consequently there is no maximum in the derivative. Tunneling spectra may be recorded for both occupied (negative voltages) and unoccupied (positive voltages) states. This allows one, in combination with model calculations and symmetry considerations, to "count" the number of electrons on the cluster.[95,96] For Au_{18} a charge of four additional electrons is found. Therefore, the proper description of the system is Au_{18}^{4-} (planar)/MgO(100).

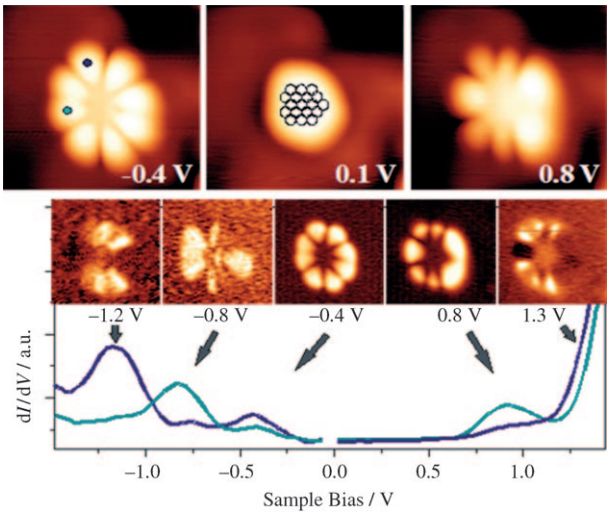

Figure 12. Set of images of Au_{18} at three different tunneling voltages and scanning tunneling spectra of Au_{18} from −2.0 eV to + 2.0 eV recorded at two different color codes top positions as marked in the image taken at −0.4 eV. For the observed maxima and the conduction bond outset conduction images have been taken.[95]

Next let us consider a larger Au island containing more than 100 Au atoms, conduction images of which are shown in Figure 13[97].

These images may well be simulated by calculations of two-dimensional Au islands containing edges and kinks. It turns out that the charge is mainly localized at the edge and preferentially at the kinks of the island. These are positions at which acceptor molecules such as CO and O_2 will bind, because the Au atoms are coordinatively unsaturated. Figure 13 shows experimental evidence for this: on the left, a topographic STM image of a randomly chosen island that was exposed to CO is shown, and on the right the same island is imaged in a mode (second derivative) that allows for detection of inelastic losses in the tunneling current.[73,97] In this particular case, the characteristic frustrated rotation of adsorbed CO at 45 meV excitation energy was probed and used for imaging. In the images the vibration, excited either by tunneling into (bright) or out of the sample (dark), is located only at the rim of the island, illustrating and iden-

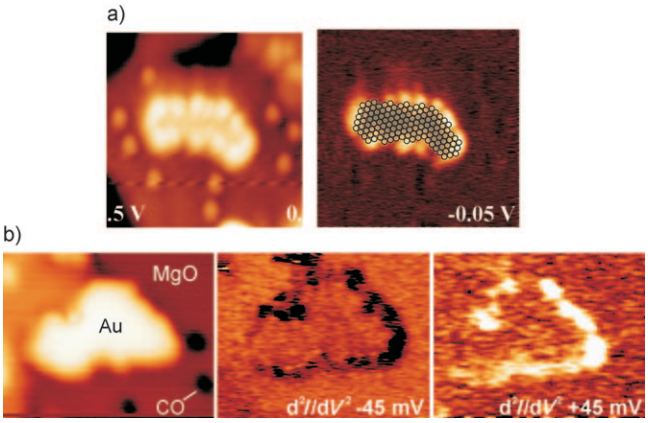

Figure 13. a) STM images of Au islands on a 3 monolayer thick MgO-(100) film before CO exposure as topographic image (left panel) and conductance image empathizing the rim (right panel). A schematic drawing of the islands topography is overlaid. b) STM image of a Au island on a trilayer MgO(100) film after exposure to CO (left panel). The two panels on the right show images taken at ± 45 mV tunneling voltage using the second derivative. These are conditions to image tunneling losses (inelastic electron tunneling spectroscopy IETS). The voltage corresponds to the hindered rotation of adsorbed CO. A prerequisite for meaningful IETS imaging is that one observes reversed contrast for opposite polarities.[73]

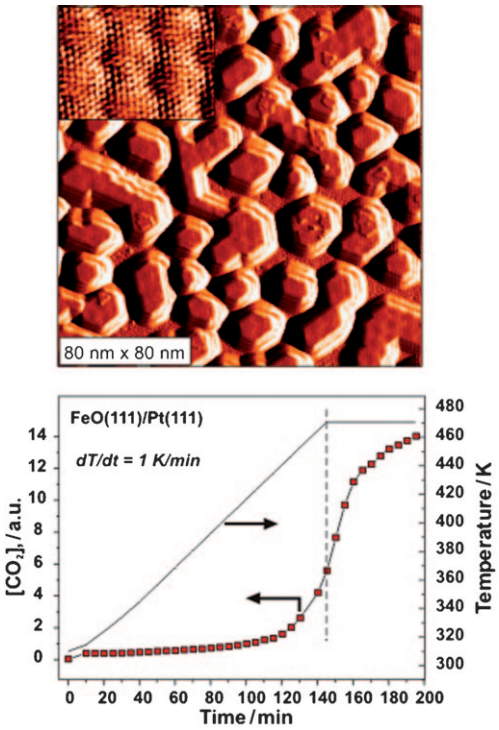

Figure 14. Top: STM image of Pt particles on $Fe_3O_4(111)$. The inset shows the atomic resolution image taken on the top facet of one of the Pt particles. Bottom: CO oxidation on FeO(111)/Pt(111) as a function of time and temperatures ($1\,K\,min^{-1}$). The dotted line indicates the time when the temperature was held constant.

tifying the preferential adsorption sites of CO molecules. One may therefore consider a scenario, when it comes to CO oxidation, in which both molecules, CO and O_2 bind to the cluster rim, and O_2 reacts either directly or after dissociation with co-adsorbed CO to give carbon dioxide.

Strong metal–support interactions (SMSI) observed with particular catalyst systems, in which metal particles (such as Pd and Pt) strongly interact with a reducible support (such as titania), and are covered by a thin oxide film upon heating to elevated temperature,[98] usually show reduced catalytic activity. The oxide film leads to a strong attenuation of adsorption capacity and, consequently, to a deactivation of the system. There have been many attempts to elucidate, even on model system, the nature of the migrating oxide film. The best studied system is $Pt/TiO_2(110)$, but even in this case the attempts have been rather unsuccessful. Very recently, we succeeded in preparing such a SMSI model system for which we are able to identify the atomic structure of the encapsulated oxide film. The system is Pt supported on a $Fe_3O_4(111)$ film grown on a Pt(111) single crystal.[16,99–101]

Figure 14 (top) shows an STM image of this system after heating to 850 K. After this treatment the CO adsorption capacity is drastically reduced, which is typical for a SMSI effect. A close look at the STM images reveals well-structured and facetted nanoparticles.

Moreover, atomically resolved images reveal corrugation that does not stem from Pt, but rather from a well-ordered double-layer FeO(111) film, well described and characterized in the literature.[102–105] As the oxide film that covers Pt particles has been identified, one may reduce the complexity of the model system by studying the properties of the bilayer FeO(111) film on a Pt(111) single crystal. Its structure has been studied in detail and characterized at the atomic level.[102–105] The $\approx 10\,\%$ misfit between the FeO(111) lattice constant and that of Pt(111) gives rise to a typical Moiré pattern in the STM image. This film is unreactive under ultrahigh vacuum conditions.[106] The situation changes, however, dramatically if one tests the system with respect to CO oxidation at ambient conditions (1 atm) in a reactor[106,107] with careful control of the relative amounts of oxygen (one part, 20 mbar), carbon monoxide (two parts, 40 mbar), and helium as buffer gas. If one ramps the temperature linear with $1\,K\,min^{-1}$ from 300 to 455 K, CO oxidation ignites at 430 K (Figure 14 bottom).

The interesting observation is that this FeO/Pt(111) system at this temperature is more than an order of magnitude more reactive than clean platinum. Usually, SMSI leads to an attenuated activity, while here we observe a strong enhancement! Further studies as a function of different gas compositions, as well as thermal desorption studies, STM investigations, and detailed DFT model calculations reveal an interesting scenario that allows us to understand this phenomenon.[101]

The scenario is depicted in Figure 15. The gas phase sets the chemical potential of the system. The shown steps are based on density functional calculations. Oxygen interacts

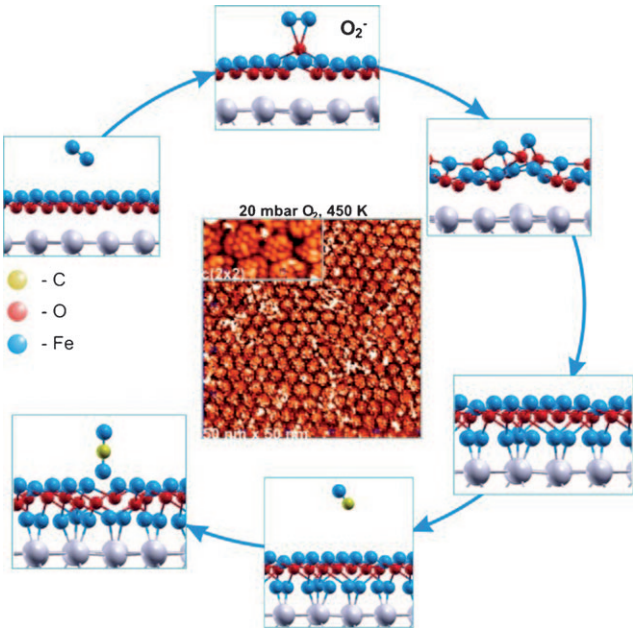

Figure 15. STM image of the active trilayer FeO_{2-x} phase. The inset shows a high resolution image.[16] The panels surrounding the image represent the individual steps in forming the active phase starting from FeO-(111)/Pt(111), and its reaction with CO to form CO_2, as revealed by density functional calculations.[16,101]

with the double layer FeO film on Pt(111) by pulling an iron atom up above the oxygen layer. This lowers the work function at the interface locally to allow for an electron transfer towards oxygen accompanied by the formation of a transient O_2^{2-} molecule, which dissociates and results, at higher oxygen coverage, in the formation of a local O-Fe-O trilayer. There is a range of experimental evidence for the existence of such a trilayer. The middle panel in Figure 15 shows an STM image of such a trilayer formed in situ at elevated O_2 pressure in a microscope.[16,101] Its appearance is mostly determined by the Moiré structure of the FeO double layer and fills 80–90% of the surface as thermal desorption spectra indicate. The images are completely consistent with the structure suggested by the calculation, although the latter does not reproduce the patched morphology due to the enormous size of the unit cell, which was impossible to implement, but necessary to fully reproduce the details. Nevertheless, if the trilayer is exposed to carbon monoxide it oxidizes the incoming CO to CO_2 by means of an Eley Rideal mechanism, leaving behind an oxygen vacancy in the film. At sufficiently high oxygen pressure the oxygen vacancy is filled again and the trilayer is sustained. If, however, the gas phase is oxygen-poor, the reaction finally stops because the trilayer is destroyed. Experimentally, we have confirmed[107] that the iron oxide film de-wets the Pt(111) surface under CO-poor reaction conditions by forming small iron oxide particles, exposing the Pt(111) surface underneath, which then determines the reactivity of the systems, in contrast to a recent study in the literature.[108] Heating the de-wetted surface in vacuum again leads to the formation of the FeO double layer, which then, at higher oxygen pressure, may be transformed into the trilayer again.

Summarizing, we are in a position to understand the phenomena in the case of ultrathin oxide films on a similar basis as in the first examples on supported small metal clusters, as the electron transfer to oxygen is the key step to initiate the process. Superficially, we may come to the conclusion that we have identified a new concept to look at catalytic systems. Closer inspection reveals that this concept has been used in the late 1940s by Cabrera and Mott[109] to understand metal oxidation and in the 1950s and 1960s by Vol′kenshtein to explain catalytic activity.[110] This concept has been revived in the late 1980s is by Frost[111] and discussed by Boudart[112] and Ponec[113] subsequently. It has only been conceptually used, as noted by Haber,[114] in electrocatalysis and the discussions of the NEMCA (non-Faradaic electrochemical modification of catalytic activity) effect by Vayenas in the 1990s[115,116] and not followed up, probably because tools to study systematically such systems at the atomic level were not applied. The time has now come!

Synopsis

Combined experimental and theoretical model studies are successful in disentangling structure–spectroscopy and structure–reactivity relationships as demonstrated for a hydrogenation and oxidation reaction. Model systems may be characterized at the atomic level experimentally, which allows for direct comparison with theoretical modeling and allows useful correlations with systems of practical relevance. The flexibility of the system is a relevant parameter that renders nanoparticle uptaken different from single crystals. Thin oxide films on metal substrates represent an interesting and promising material combination. It is possible to use known concepts from semiconductor physics to understand the underlying principles, taking the flexibility of the system into account, and to use them to design model systems to get insight into elementary questions in catalysis. In both examples discussed electron transfer determines reactivity. It is quite possible to think about material combinations that would favor electron transfer for specific molecules and induce specific and selective reactions. Maybe that these new (old) concepts could be used as a guideline to design catalysts and also to understand systems that have been controversially discussed in the literature.[117–120] One such case is the increased activity of Ru(0001) surfaces, claimed to be due to the formation of RuO_2 on the surface. It is, however, possible that the formation of a thin oxide film that exhibits appropriate properties promotes the reaction. It is important to note that it is crucial to have appropriate experimental techniques at ones disposal to look at this. The design of a useful set of experimental techniques is a key goal of experimental research.

Acknowledgements

I would like to thank my co-workers and students for their excellent work over almost three decades. Their names appear in the references and I am grateful to them for spending time in my laboratory and working with me. Many fruitful and illuminating discussions with partners in theory: Hannu Häkkinen, Gianfranco Pacchioni, and Joachim Sauer are gratefully acknowledged. We thank the German Science Foundation through the Cluster of Excellence UniCat and the Fonds der Chemischen Industrie for support. I am delighted to have been part of an organization—the Max-Planck Society—that gave me the freedom to follow my ideas and dreams without many administrative constraints that other researchers have to endure.

[1] *Handbook of Heterogeneous Catalysis, Vol. 4*, (Eds.: G. Ertl, H. Knözinger, F. Schüth, J. Weitkamp), Wiley-VCH, Weinheim, **2008**.
[2] C. R. Henry, *Surf. Sci. Rep.* **1998**, *31*, 231.
[3] C. T. Campbell, *Surf. Sci. Rep.* **1997**, *27*, 1.
[4] D. W. Goodman, *Surf. Rev. Lett.* **1995**, *2*, 9.
[5] H.-J. Freund, G. Pacchioni, *Chem. Soc. Rev.* **2008**, *37*, 2224.
[6] T. Risse, S. Shaikhutdinov, N. Nilius, M. Sterrer, H.-J. Freund, *Acc. Chem. Res.* **2008**, *41*, 949.
[7] N. Nilius, *Surf. Sci. Rep.* **2009**, *64*, 595.
[8] N. Nilius, T. Risse, S. Schauermann, S. Shaikhutdinov, M. Sterrer, H. J. Freund, *Top. Catal.* **2010**, unpublished results.
[9] H.-J. Freund, *Angew. Chem.* **1997**, *109*, 444; *Angew. Chem. Int. Ed. Engl.* **1997**, *36*, 452.
[10] H.-J. Freund, *Surf. Sci.* **2002**, *500*, 271.
[11] H.-J. Freund, H. Kuhlenbeck, V. Staemmler, *Rep. Prog. Phys.* **1996**, *59*, 283.
[12] H.-J. Freund, D. W. Goodman in *Handbook of Heterogeneous Catalysis*, 2nd ed. (Eds.: G. Ertl, H. Knözinger, F. Schüth, J. Weitkamp), Wiley-VCH, Weinheim, **2007**.
[13] G. Ertl, H.-J. Freund, *Phys. Today* **1999**, *52*, 32.
[14] J.-H. Fischer-Wolfahrt, J. A. Farmer, J. M. Flores-Camacho, A. Genest, I. V. Yudanov, N. Rösch, C. T. Campbell, S. Schauermann, H. J. Freund, *Phys. Rev. B* **2010**, *81*, 241416.>
[15] M. Lewandowski, Y. N. Sun, Z. H. Qin, S. Shaikhutdinov, H. J. Freund, *Appl. Catal. B* **2010**, DOI: 10.1016/j.apcata.2010.04.030.
[16] M. Lewandowski, Ph.D. thesis, Technical University (Berlin), **2010**.
[17] R. Meyer, S. Shaikhutdinov, H. J. Freund, *Z. Phys. Chem.* **2004**, *218*, 905.
[18] K. H. Hansen, T. Worren, S. Stempel, E. Lægsgaard, M. Bäumer, H. J. Freund, F. Besenbacher, I. Stensgaard, *Phys. Rev. Lett.* **1999**, *83*, 4120.
[19] D. Mulugeta, K. H. Kim, K. Watanabe, D. Menzel, H.-J. Freund, *Phys. Rev. Lett.* **2008**, *101*, 146103.
[20] K. Watanabe, Y. Matsumoto, M. Kampling, K. Al-Shamery, H.-J. Freund, *Angew. Chem.* **1999**, *111*, 2328; *Angew. Chem. Int. Ed.* **1999**, *38*, 2192.
[21] A. Stuck, C. E. Wartnaby, Y. Y. Yeo, J. T. Stuckless, N. Al-Sarraf, D. A. King, *Surf. Sci.* **1996**, *349*, 229.
[22] D. E. Starr, C. T. Campbell, *J. Phys. Chem. B* **2001**, *105*, 3776.
[23] I. V. Yudanov, A. V. Matveev, K. M. Neyman, N. Rösch, *J. Am. Chem. Soc.* **2008**, *130*, 9342.
[24] B. Brandt, W. Ludwig, J.-H. Fischer, J. Libuda, F. Zaera, S. Schauermann, *J. Catal.* **2009**, *265*, 191.
[25] B. Brandt, J.-H. Fischer, W. Ludwig, J. Libuda, F. Zaera, S. Schauermann, H.-J. Freund, *J. Phys. Chem. C* **2008**, *112*, 11408.
[26] M. Wilde, K. Fukutani, W. Ludwig, B. Brandt, J.-H. Fischer, S. Schauermann, H. J. Freund, *Angew. Chem.* **2008**, *120*, 9430; *Angew. Chem. Int. Ed.* **2008**, *47*, 9289.
[27] K. M. Neyman, S. Schauermann, *Angew. Chem.* **2010**, *122*, 4851; *Angew. Chem. Int. Ed.* **2010**, *49*, 4743.
[28] W. Ludwig, A. Savara, S. Schauermann, *Dalton Trans.* **2010**, DOI: 10.1039/c003133j.
[29] G. Rupprechter, H. Unterhalt, M. Morkel, P. Galletto, L. Hu, H.-J. Freund, *Surf. Sci.* **2002**, *502–503*, 109.
[30] G. Ertl, *Reactions at Solid Surfaces*, Wiley, New York, **2009**.
[31] G. Somorjai, Y. Li, *Introduction to Surface Chemistry and Catalysis*, 2nd ed., Wiley, New York, **2010**.
[32] A. M. Doyle, S. Shaikhutdinov, S. D. Jackson, H.-J. Freund, *Angew. Chem.* **2003**, *115*, 5398; *Angew. Chem. Int. Ed.* **2003**, *42*, 5240.
[33] A. M. Doyle, S. Shaikhutdinov, H. J. Freund, *Angew. Chem.* **2005**, *117*, 635; *Angew. Chem. Int. Ed.* **2005**, *44*, 629.
[34] T. Schalow, M. Laurin, B. Brandt, S. Schauermann, S. Guimond, H. Kuhlenbeck, D. Starr, S. Shaikhutdinov, J. Libuda, H. J. Freund, *Angew. Chem.* **2005**, *117*, 7773; *Angew. Chem. Int. Ed.* **2005**, *44*, 7601.
[35] D. Teschner, J. Borsodi, A. Wootsch, Z. Révay, M. Hävecker, A. Knop-Gericke, S. D. Jackson, R. Schlögl, *Science* **2008**, *320*, 86.
[36] W. Ludwig, A. Savara, S. Schauermann, H. J. Freund, *ChemPhys Chem* **2010**, DOI: 10.1002/cphc.201000355.
[37] J. A. Dumasic, D. F. Rudd, L. M. Aparicio, *The Microkinetics of Heterogeneous Catalysis*, ACS, Washington, **1993**.
[38] J. Horiuti, M. Polanyi, *Trans. Faraday Soc.* **1934**, *30*, 1164.
[39] F. Zaera, *Prog. Surf. Sci.* **2001**, *69*, 1.
[40] Z. Ma, F. Zaera, *Surf. Sci. Rep.* **2006**, *61*, 229.
[41] F. Zaera, *Chem. Rev.* **1995**, *95*, 2651.
[42] F. Zaera, *Acc. Chem. Res.* **1992**, *25*, 260.
[43] F. Zaera, *Langmuir* **1996**, *12*, 88.
[44] M. Wilde, K. Fukutani, M. Naschitzki, H. J. Freund, *Phys. Rev. B* **2008**, *77*, 113412.
[45] I. E. Wachs, *Catal. Today* **2005**, *100*, 79.
[46] N. Magg, J. B. Giorgi, T. Schroeder, M. Bäumer, H. J. Freund, *J. Phys. Chem. B* **2002**, *106*, 8756.
[47] N. Magg, B. Immaraporn, J. Giorgi, T. Schroeder, M. Bäumer, J. Döbler, Z. Wu, E. Kondratenko, M. Cherian, M. Baerns, P. C. Stair, J. Sauer, H.-J. Freund, *J. Catal.* **2004**, *226*, 88.
[48] S. Guimond, M. Abu Haija, S. Kaya, J. Lu, J. Weissenrieder, S. Shaikhutdinov, H. Kuhlenbeck, H.-J. Freund, J. Döbler, J. Sauer, *Top. Catal.* **2006**, *38*, 117.
[49] S. Kaya, Y. N. Sun, J. Weissenrieder, D. Stacchiola, S. Shaikhutdinov, H. J. Freund, *J. Phys. Chem. C* **2007**, *111*, 5337.
[50] S. Guimond, J. M. Sturm, D. Göbke, Y. Romanyshyn, M. Naschitzki, H. Kuhlenbeck, H.-J. Freund, *J. Phys. Chem. C* **2008**, *112*, 11835.
[51] Y. Romanyshyn, S. Guimond, H. Kuhlenbeck, S. Kaya, R. P. Blum, H. Niehus, S. Shaikhutdinov, M. Simic-Milosevic, N. Nilius, H. J. Freund, M. V. Ganduglia-Pirovano, R. Fortrie, J. Döbler, J. Sauer, *Top. Catal.* **2008**, *50*, 106.
[52] D. Göbke, Y. Romanyshyn, S. Guimond, J. M. Sturm, H. Kuhlenbeck, J. Döbler, U. Reinhardt, M. V. Ganduglia-Pirovano, J. Sauer, H. J. Freund, *Angew. Chem.* **2009**, *121*, 3750; *Angew. Chem. Int. Ed.* **2009**, *48*, 3695.
[53] J. M. Sturm, D. Göbke, H. Kuhlenbeck, J. Döbler, U. Reinhardt, M. V. Ganduglia-Pirovano, J. Sauer, H. J. Freund, *Phys. Chem. Chem. Phys.* **2009**, *11*, 3290.
[54] M. Baron, O. Bondarchuk, D. Stacchiola, S. Shaikhutdinov, H. J. Freund, *J. Phys. Chem. C* **2009**, *113*, 6042.
[55] H. L. Abbott, A. Uhl, M. Baron, Y. Lei, R. J. Meyer, D. J. Stacchiola, O. Bondarchuk, S. Shaikhutdinov, H. J. Freund, *J. Catal.* **2010**, *272*, 82.
[56] M. V. Ganduglia-Pirovano, C. Popa, J. Sauer, H. Abbott, A. Uhl, M. Baron, D. Stacchiola, O. Bondarchuk, S. Shaikhutdinov, H.-J. Freund, *J. Am. Chem. Soc.* **2010**, *132*, 2345.
[57] J. L. Lu, H. J. Gao, S. Shaikhutdinov, H. J. Freund, *Surf. Sci.* **2006**, *600*, 5004.
[58] D. R. Mullins, P. V. Radulovic, S. H. Overbury, *Surf. Sci.* **1999**, *429*, 186.
[59] J. Döbler, M. Pritzsche, J. Sauer, *J. Am. Chem. Soc.* **2005**, *127*, 10861.
[60] X. Rozanska, R. M. Fortrie, J. Sauer, *J. Phys. Chem. C* **2007**, *111*, 6041.
[61] J. Sauer, J. Döbler, *Dalton Trans.* **2004**, 3116.
[62] H. Y. Kim, H. M. Lee, R. G. S. Pala, V. Shapovalov, H. Metiu, *J. Phys. Chem. C* **2008**, *112*, 12398.

[63] M. V. Ganduglia-Pirovano, J. L. F. Da Silva, J. Sauer, *Phys. Rev. Lett.* **2009**, *102*, 026101.
[64] M. Sterrer, E. Fischbach, T. Risse, H.-J. Freund, *Phys. Rev. Lett.* **2005**, *94*, 186101.
[65] M. Sterrer, E. Fischbach, M. Heyde, N. Nilius, H. P. Rust, T. Risse, H. J. Freund, *J. Phys. Chem. B* **2006**, *110*, 8665.
[66] M. Sterrer, M. Heyde, M. Novicki, N. Nilius, T. Risse, H.-P. Rust, G. Pacchioni, H.-J. Freund, *J. Phys. Chem. B* **2005**, *109*, 46.
[67] K. M. Neyman, C. Inntam, A. V. Matveev, V. A. Nasluzov, N. Rösch, *J. Am. Chem. Soc.* **2005**, *127*, 11652.
[68] Z. Yan, S. Chinta, A. A. Mohamed, J. P. Fackler, D. W. Goodman, *J. Am. Chem. Soc.* **2005**, *127*, 1604.
[69] G. Pacchioni, S. Sicolo, C. Di Valentin, M. Chiesa, E. Giamello, *J. Am. Chem. Soc.* **2008**, *130*, 8690.
[70] T. Trevethan, A. Shluger, *Nanotechnology* **2009**, *20*, 264019.
[71] T. König, G. H. Simon, H. P. Rust, G. Pacchioni, M. Heyde, H. J. Freund, *J. Am. Chem. Soc.* **2009**, *131*, 17544.
[72] T. König, G. H. Simon, U. Martinez, L. Giordano, G. Pacchioni, M. Heyde, H.-J. Freund, *ACS Nano* **2010**, *4*, 2510.
[73] X. Lin, B. Yang, H. M. Benia, P. Myrach, M. Yulikov, A. Aumer, M. Brown, M. Sterrer, O. Bondarchuk, E. Kieseritzky, J. Rocker, T. Risse, H. Gao, N. Nilius, H. J. Freund, *J. Am. Chem. Soc.* **2010**, *132*, 7745.
[74] H. M. Benia, P. Myrach, A. Gonchar, T. Risse, M. Nilius, H. J. Freund, *Phys. Rev. B* **2010**, *81*, 241415.
[75] M. Chiesa, M. C. Paganini, E. Giamello, D. M. Murphy, C. Di Valentin, G. Pacchioni, *Acc. Chem. Res.* **2006**, *39*, 861.
[76] A. Fielicke, P. Gruene, G. Meijer, D. M. Rayner, *Surf. Sci.* **2009**, *603*, 1427.
[77] P. Gruene, D. M. Rayner, B. Redlich, A. F. G. v. d. Meer, J. T. Lyon, G. Meijer, A. Fielicke, *Science* **2008**, *321*, 674.
[78] I. Swart, F. M. F. de Groot, B. M. Weckhuysen, D. M. Rayner, G. Meijer, A. Fielicke, *J. Am. Chem. Soc.* **2008**, *130*, 2126.
[79] A. Fielicke, G. von Helden, G. Meijer, D. B. Pedersen, B. Simard, D. M. Rayner, *J. Chem. Phys.* **2006**, *124*, 194305.
[80] A. Fielicke, G. von Helden, G. Meijer, D. B. Pedersen, B. Simard, D. M. Rayner, *J. Am. Chem. Soc.* **2005**, *127*, 8416.
[81] M. Sterrer, M. Yulikov, T. Risse, H. J. Freund, J. Carrasco, F. Illas, C. Di Valentin, L. Giordano, G. Pacchioni, *Angew. Chem.* **2006**, *118*, 2695; *Angew. Chem. Int. Ed.* **2006**, *45*, 2633.
[82] U. Heiz, F. Vanolli, L. Trento, W. D. Schneider, *Rev. Sci. Instrum.* **1997**, *68*, 1986.
[83] U. Heiz, A. Sanchez, S. Abbet, W.-D. Schneider, *J. Am. Chem. Soc.* **1999**, *121*, 3214.
[84] U. Heiz, A. Sanchez, S. Abbet, W. D. Schneider, *Chem. Phys.* **2000**, *262*, 189.
[85] U. Heiz, W.-D. Schneider, *J. Phys. D* **2000**, *33*, R85.
[86] L. Giordano, U. Martinez, S. Sicolo, G. Pacchioni, *J. Chem. Phys.* **2007**, *127*, 144713.
[87] M. Haruta, *Cattech* **2002**, *6*, 102.
[88] G. J. Hutchings, M. Brust, H. Schmidbaur, *Chem. Soc. Rev.* **2008**, *37*, 1759.
[89] R. Meyer, C. Lemire, S. Shaikhutdinov, H.-J. Freund, *Gold Bull.* **2004**, *37*, 72.
[90] M. Sterrer, T. Risse, L. Giordano, M. Heyde, N. Nilius, H. P. Rust, G. Pacchioni, H.-J. Freund, *Angew. Chem.* **2007**, *119*, 8858; *Angew. Chem. Int. Ed.* **2007**, *46*, 8703.
[91] M. Sterrer, T. Risse, U. Martinez Pozzoni, L. Giordano, M. Heyde, H.-P. Rust, G. Pacchioni, H.-J. Freund, *Phys. Rev. Lett.* **2007**, *98*, 096107.
[92] M. Sterrer, T. Risse, M. Heyde, H.-P. Rust, H.-J. Freund, *Phys. Rev. Lett.* **2007**, *98*, 206103.
[93] V. Simic-Milosevic, M. Heyde, N. Nilius, T. Koenig, H. P. Rust, M. Sterrer, T. Risse, H. J. Freund, L. Giordano, G. Pacchioni, *J. Am. Chem. Soc.* **2008**, *130*, 7814.
[94] V. Simic-Milosevic, M. Heyde, X. Lin, T. König, H.-P. Rust, M. Sterrer, T. Risse, N. Nilius, H.-J. Freund, L. Giordano, G. Pacchioni, *Phys. Rev. B* **2008**, *78*, 235429.
[95] X. Lin, N. Nilius, H. J. Freund, M. Walter, P. Frondelius, K. Honkala, H. Häkkinen, *Phys. Rev. Lett.* **2009**, *102*, 206801.
[96] N. Nilius, M. V. Ganduglia-Pirovano, V. Brázdová, M. Kulawik, J. Sauer, H. J. Freund, *Phys. Rev. Lett.* **2008**, *100*, 096802.
[97] X. Lin, N. Nilius, M. Sterrer, P. Koskinen, H. Häkkinen, H.-J. Freund, *Phys. Rev. B* **2010**, *81*, 153406.
[98] F. C. M. J. M. Van Delft, B. E. Nieuwenhuys, *Solid State Ionics* **1985**, *16*, 233.
[99] Z. H. Qin, M. Lewandowski, Y. N. Sun, S. Shaikhutdinov, H. J. Freund, *J. Phys. Chem. C* **2008**, *112*, 10209.
[100] Z. H. Qin, M. Lewandowski, Y. N. Sun, S. Shaikhutdinov, H. J. Freund, *J. Phys. Condens. Matter* **2009**, *21*, 134019.
[101] Y.-N. Sun, L. Giordano, J. Goniakowski, M. Lewandowski, Z.-H. Qin, C. Noguera, S. Shaikhutdinov, G. Pacchioni, H.-J. Freund, *Angew. Chem.* **2010**, *122*, 4520; *Angew. Chem. Int. Ed.* **2010**, *49*, 4418.
[102] H. C. Galloway, J. J. Benítez, M. Salmeron, *Surf. Sci.* **1993**, *298*, 127.
[103] W. Weiss, A. Barbieri, M. A. Van Hove, G. A. Somorjai, *Phys. Rev. Lett.* **1993**, *71*, 1848.
[104] G. H. Vurens, M. Salmeron, G. A. Somorjai, *Surf. Sci.* **1988**, *201*, 129.
[105] G. H. Vurens, V. Maurice, M. Salmeron, G. A. Somorjai, *Surf. Sci.* **1992**, *268*, 170.
[106] Y. N. Sun, Z. H. Qin, M. Lewandowski, E. Carrasco, M. Sterrer, S. Shaikhutdinov, H. J. Freund, *J. Catal.* **2009**, *266*, 359.
[107] Y. N. Sun, Z. H. Qin, M. Lewandowski, S. Kaya, S. Shaikhutdinov, H. J. Freund, *Catal. Lett.* **2008**, *126*, 31.
[108] Q. Fu, W.-X. Li, Y. Yao, L. Hongyang, Q. Fu, H.-Y. Su, D. Ma, X.-K. Gu, L. Chen, Z. Wang, H. Zhang, B. Wang, X. Bao, *Science* **2010**, *328*, 1141.
[109] N. Cabrera, N. F. Mott, *Rep. Prog. Phys.* **1949**, *12*, 163.
[110] F. F. Vol′kenshtein, *Russ. Chem. Rev.* **1966**, *35*, 537.
[111] J. C. Frost, *Nature* **1988**, *334*, 577.
[112] M. Boudart, *Catal. Lett.* **1992**, *13*, 153.
[113] V. Ponec, *Catal. Lett.* **1991**, *11*, 249.
[114] B. Grzybowska-Swierkosz, J. Haber, *Annu. Rep. Prog. Chem. Sect. C* **1994**, *91*, 395.
[115] C. G. Vayenas, C. G. Koutsodontis, *J. Chem. Phys.* **2008**, *128*, 182506.
[116] M. N. Tsampas, F. M. Sapountzi, C. G. Vayenas, *Catal. Today* **2009**, *146*, 351.
[117] C. H. F. Peden, D. W. Goodman, *J. Phys. Chem.* **1986**, *90*, 1360.
[118] H. Over, M. Muhler, *Prog. Surf. Sci.* **2003**, *72*, 3.
[119] K. Reuter, C. Stampfl, V. Ganduglia-Pirovano, M. Scheffler, *Chem. Phys. Lett.* **2002**, *352*, 311.
[120] D. Rosenthal, F. Girgsdies, O. Timpe, R. Blume, G. Weinberg, D. Teschner, R. Schlögl, *J. Phys. Chem.* **2009**, *233*, 183.
[121] H. Conrad, G. Ertl, J. Koch, E. E. Latta, *Surf. Sci.* **1974**, *43*, 462.

Published online: July 28, 2010

